



ELSEVIER

Surface Science 370 (1997) 166–178

surface science

The surface chemistry of metal–oxygen interactions: a first-principles study of O:Rh(110)

Kurt Stokbro^{a,*}, Stefano Baroni^{a,b}

^a *Istituto Nazionale di Fisica della Materia (INFN) and Scuola Internazionale Superiore di Studi Avanzati (SISSA), via Beirut 2/4, I-34014 Trieste, Italy*

^b *Centre Européen de Calcul Atomique et Moléculaire (CECAM), ENS-Lyon, 46 Allée d'Italie, F-69007 Lyon, France*

Received 14 May 1996; accepted for publication 19 July 1996

Abstract

We report on a computational study of the clean and oxygen-covered Rh(110) surface, based on density-functional theory within the local-density approximation. We have used plane-wave basis sets and Vanderbilt ultra-soft pseudopotentials. For the clean surface, we present results for the equilibrium structure, surface energy and surface stress of the unreconstructed and (1×2) reconstructed structures. For the oxygen-covered surface we have performed a geometry optimization at 0.5, 1, and 2 monolayer oxygen coverages, and we present results for the equilibrium configurations, workfunctions and oxygen chemisorption energies. At half monolayer coverage, we find that oxygen induces a (1×2) reconstruction of the surface, while at one monolayer coverage the chemisorption energy is highest for the unreconstructed surface. Our results are rationalized by a simple tight-binding description of the interaction between the O 2p orbitals and the metal valence states. The resulting bonds are stronger when established with low coordinated metal atoms, and give rise to an effective adsorbate–adsorbate interaction when two oxygen atoms are bound to the same metal orbital.

Keywords: Adatoms; Density functional calculations; Oxygen; Rhodium; Surface energy; Surface stress

1. Introduction

Oxygen is known to form strong bonds with metal surfaces, and the oxygen–metal interaction is one of the key elements in many technologically relevant catalytic reactions, such as the oxidation of carbon or the reduction of nitrogen from their mono-oxides, occurring in catalytic mufflers. As a first step towards an understanding of the microscopic mechanisms responsible for the catalytic activity of some transition-metal surfaces, we pre-

sent in this paper a first-principles study of the interaction between oxygen and the Rh(110) surface. From the calculations we extract simple chemical models of the metal–oxygen interaction, which we believe to be of general relevance for adsorbate–metal systems.

The structure of the oxygen covered Rh(110) surface strongly depends on the oxygen coverage [1–4]. At very low coverages oxygen is believed to occupy four-fold long-bridge sites. At a certain critical coverage, $\theta = \theta_c \lesssim 0.5$ monolayers, oxygen starts to induce a (1×2) missing-row reconstruction of the surface, where the oxygen atoms occupy every second three-fold site along the closed-packed top row. At $\theta = 0.5$ the reconstruction is

* Corresponding author. Present address: Mikroelektronik Centret, Danmarks Tekniske Universitet, Bygning 345Ø, DK-2800 Lyngby, Denmark. e-mail: stokbro@mic.dtu.dk

fully developed, and at higher coverages the surface starts to deconstruct. At $\theta=1$ the rhodium substrate is again unreconstructed and oxygen forms a (2×1) pattern. Our calculations, performed at $\theta=0.5$, 1 and 2 support, for these coverages, the picture given above.

From our self-consistent calculations we have extracted a simple chemical model of the oxygen–metal interaction. From the model we identify a strong adsorbate–adsorbate interaction when two oxygen atoms are bound to the same metal orbital, and we discuss this effect in connection with the calculations at $\theta=1$. We also show that the model predicts stronger oxygen bonds with low coordinated metal atoms, and this is the force which drives the oxygen-induced reconstruction at $\theta=0.5$.

The paper is organized as follows: In Section 2 we briefly describe the pseudopotential method used for the calculations, and present our results for bulk Rh; in Section 3 we report on our calculations for the clean Rh(110) surface, and in Section 4 on the results for the oxygen covered surface; in Section 5 we present the model of the rhodium–oxygen bond; finally, Section 6 contains our conclusions.

2. Technical details and results for bulk Rh

Our calculations are based on density-functional theory within the local-density approximation (LDA) [5,6]. Although the LDA is known to overestimate cohesive and chemisorption energies, it has long since proven to be rather reliable as far as relative energies between different bulk and surface geometries are concerned [7]. A recent study of oxygen chemisorption on Al(111) [8] showed that the LDA and the generalized gradient approximation (GGA) of Ref. [9] gave similar results for oxygen chemisorption geometries and relative chemisorption energies. In our study we only apply the LDA, however, whenever possible comparisons with experiment for the calculated oxygen chemisorption geometries and relative chemisorption energies show excellent agreement, and we therefore find the use of the LDA appropriate for the problems addressed in this paper.

The electron-gas data used to implement the LDA are those by Ceperley and Alder [10] as parameterized by Perdew and Zunger [11]. The single-particle Kohn–Sham equations are solved using the plane-wave (PW) pseudopotential method. Isolated surfaces are modelled by slabs in the supercell geometry. Due to the well known *hardness* of norm-conserving pseudopotentials for first-row elements – such as O – and, to a lesser extent, for second-transition-row atoms – such as Rh –, the use of *ultrasoft* (US) potentials [12] is mandatory in order to keep the size of the PW basis sets manageable for the large supercells necessary to model the surface. The oxygen US pseudopotential is essentially identical to that of Ref. [13] with a core radius of 1.3 a.u. For rhodium we have used a newly developed variant of the Vanderbilt scheme [12], where the norm conservation is released only for those angular-momentum channels which would otherwise require very hard potentials (the *d*-channel only in the present case) [14]. The pseudopotential is constructed from a scalar-relativistic all-electron calculation, and it includes the 4d-, 5s- and 5p-valence states, for which we used the core radii 1.6, 2.53 and 2.53 a.u. respectively. The 4d and 5s orbitals were constructed in the atomic reference configuration $4d^8 5s^1$, while the 5p orbital was taken from the reference configuration $4d^7 5s^{0.75} 5p^{0.25}$. Basis sets including PWs up to a kinetic energy cutoff $E_{\text{cut}} \approx 25$ –30 Ry yield very accurate results for both elements [13,14]. We finally decided to adopt a cutoff of 30 Ry. This choice allows one to neglect the effects of the finiteness of the basis sets even in those instances, such as the calculation of the stress tensor [15], which are very sensitive to it.

Brillouin-zone (BZ) integrations are performed using the Gaussian-smearing special-point technique [16]. We have found that the bulk properties are well converged using a Gaussian broadening of 0.3 eV and a Monkhorst–Pack (444) mesh [17], which corresponds to 10 k points in the irreducible wedge of the BZ. In order to test the convergence of our numerical BZ integrations, in many cases we have made refined test calculations with a Gaussian broadening of 0.15 eV and a correspondingly finer mesh. No significant differences were found in any of the cases examined. This fast

convergence with respect to BZ sampling is due to the relatively smooth Density of States (DOS) at the Fermi energy, as shown in Fig. 1. In this figure we also show the projection of the DOS onto individual atomic orbitals. There are 8.0 electrons per atom in the d bands, while the remaining electron has mixed s and p character.

The calculated lattice constant is $a_0 = 3.81$ Å and the bulk modulus $B = 3.17$ Mbar, in good agreement with the experimental values (3.80 and 2.76 respectively) [18]. The overestimation of the bulk modulus is also found in relativistic all-electron calculations, and therefore it is not due to the use of pseudopotentials, but rather due to the LDA [14]. The quality of the agreement between theory and experiment is of the same order as found for most LDA calculations for metals and semiconductors.

3. The clean Rh(110) surface

The structural properties of the clean unreconstructed and (1×2) reconstructed surfaces have been studied by minimizing the supercell total energy with respect to atomic positions, using the

Broyden–Fletcher–Goldfarb–Shanno minimization technique [19]. The value of the workfunction was estimated by taking the difference between the calculated Fermi level and the electrostatic potential in the middle of the vacuum region.

We denote the repeated-cell slab geometry by the notation $(N+M)$, where N is the number of atomic layers in the slab, and M the thickness of the vacuum region, in units of the interlayer spacing normal to the surface. Different supercells – going from $(5+5)$ to $(9+5)$ and $(7+7)$ – were checked in order to test the convergence of our results. We found no difference between the results obtained for $M=5$ and $M=7$, and also the dependence upon N is very small. As for k -point sampling we tested a Gaussian broadening of 0.3 eV and a Monkhorst–Pack (442) mesh [17] – which corresponds to 4 k points in the irreducible wedge of the supercell BZ – and a Gaussian broadening of 0.15 eV in conjunction with a (882) mesh. We find that the error introduced by using a (442) mesh is of the same order as the finite size error by using a $(7+5)$ cell.

In Table 1 we present the calculated atomic positions, workfunction, surface energy and surface stress for the relaxed Rh(110) surface, and compare

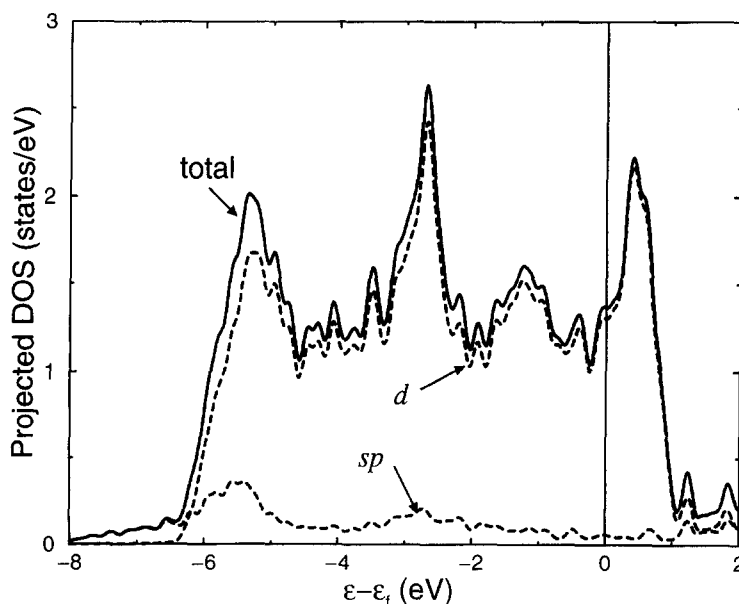


Fig. 1. The rhodium bulk DOS (solid line) and its projection onto sp and d atomic orbitals (dotted lines).

Table 1

Interlayer relaxations (Δd_{12} , Δd_{23} , Δd_{34}), work function (W), surface energy (σ), and surface tensions (σ_{xx} , σ_{yy}) of the Rh(110) surface (the x axis is oriented in the (110) direction)

	Δd_{12} (%)	Δd_{23} (%)	Δd_{34} (%)	W (eV)	σ (eV \AA^{-2})	σ_{xx} (eV \AA^{-2})	σ_{yy} (eV \AA^{-2})
Experiment	$-7(1)^a$	$2(1)^a$		5.1^b			
LDA Unrelaxed				$5.13(5)$	$0.198(5)$	$0.28(2)$	$0.25(2)$
LDA relaxed	$-9.7(5)$	$3.6(8)$	$-2.2(9)$	$5.14(5)$	$0.191(5)$	$0.20(2)$	$0.12(2)$

The first row shows the available experimental data, while the second row shows the calculated values before surface relaxation, and the the third row after relaxation. The numbers in parenthesis indicate an estimate of the numerical error on the last displayed digit, due to the super-cell size and k -point sampling.

^aFrom Ref. [20].

^bFrom Ref. [40].

them with the corresponding values obtained for the unrelaxed surface. The values were obtained from the $(7+5)$ cell, with the (442) k -point mesh, and the error estimate was based on calculations performed with the (882) mesh and/or $(9+5)$ supercell geometry. We observe a large inward relaxation of the first layer, analogous to what usually occurs at other open surfaces. However, the calculated relaxation is almost one and a half times as large as the value obtained from LEED structural analysis [20]. Since the calculated bulk modulus is 10% too large, one could have expected an overestimate of the surface relaxations, but we also note that the experimental value of [20] is probably too small, since these authors only included relaxations of the first two surface layers in their structural model. We find that the surface relaxations strongly reduce the surface tension, indicating that the surface relaxation and surface tension are determined by the same driving force. This is in qualitative agreement with the Effective-Medium Theory of Refs. [21,22], according to which an inward relaxation of the outermost atomic plane would decrease the surface energy by increasing the electron density at surface atoms.

We now turn to the electronic structure of the Rh(110) surface. In Fig. 2a we compare the projections of the DOS (PDOS) onto the surface atomic layer and onto an atomic layer in the bulk. The PDOS was constructed using the (882) mesh and a Gaussian broadening of 0.15 eV, and we noted that the PDOS constructed from a (442) mesh had the same features. The main difference is the decreased band width and upward shift of the

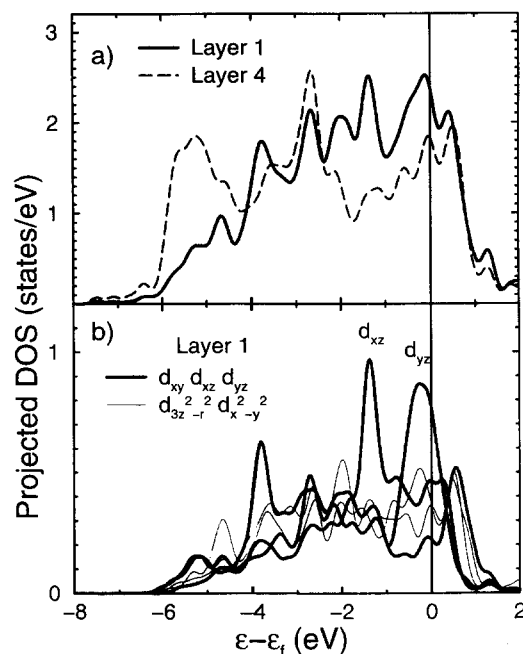


Fig. 2. The DOS of the Rh(110) surface projected onto: (a) layer 1 (solid line) and layer 4 (dashed line); (b) The five d orbitals of layer 1.

band centre of the first layer PDOS. This effect is in qualitative agreement with the \sqrt{N} scaling of the band width, where N is the coordination number, predicted by a simple one-band tight-binding model. In Fig. 2b we show the PDOS of the surface d-orbitals, and we now see the appearance of resonances in the spectrum caused by the broken metal-metal bonds. The strongest resonance is caused by the yz orbital, and the signifi-

cance of this orbital is that it can only form weak δ bonds along the (110) surface row. In Section 5 we will discuss the chemical bonding between oxygen and the rhodium surface and we will hint that these resonances give an important contribution to the chemisorption energy. In analogy to the terminology adopted for semiconductors, we will call these resonances *metallic dangling bonds*.

Finally, we have considered the (1×2) missing-row reconstructed surface shown in Fig. 3. This surface structure is not found to be stable in nature, but it can be produced in a metastable state by first treating the surface with oxygen which afterwards is removed with a strong reductant like CO [2]. Table 2 shows the calculated properties of the relaxed reconstructed surface, and the reported results were obtained with a $(7+5)$ layer slab and a (882) k -point mesh. The workfunction, surface energy and surface stress are given relative to the relaxed unreconstructed surface, i.e. the mean of a $(7+5)$ layer and a $(5+7)$ layer slab calculation with (882) k -point mesh, and the error estimates are obtained from a $(6+4)$ layer slab calculation of the reconstructed surface.

Generally the relaxations are in good agreement

with those obtained from the LEED structural analysis of Ref. [2], and we predict an increase in the surface energy compared to the unreconstructed surface of ≈ 0.1 eV/ (1×2) cell, while there is no significant difference in the surface stress.

4. The oxygen-covered Rh(110) surface

In this section we present calculations for the Rh(110) surface with a coverage of 0.5, 1, and 2 oxygen monolayers. For the calculations we used a $(7+5)$ supercell, with the oxygen atoms introduced on both sides of the slab, keeping inversion symmetry. Fig. 4 shows the relaxed structures of the geometries we have considered, and in Table 3 we report some key values of each chemisorption geometry. To estimate the finite size effects we have in each case recalculated the structure for a $(5+5)$ layer slab, and most calculations have also been redone with a (882) k -point mesh. Based on these calculations we have made the error estimates in Table 3. The dominating error is due to finite-size effects, caused by the charge transfer from the

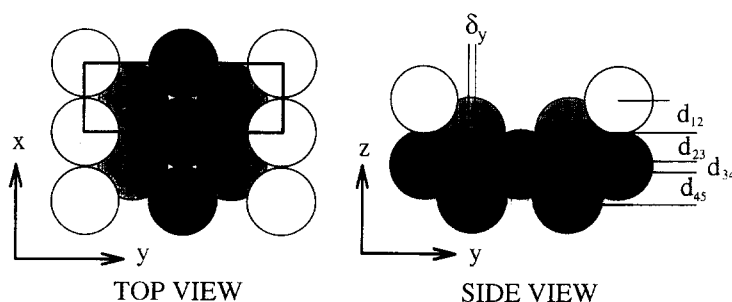


Fig. 3. The geometry of the (1×2) missing row reconstruction.

Table 2
Experimental and calculated surface properties of the (1×2) reconstructed surface

	δ_y (%)	Δd_{12} (%)	Δd_{23} (%)	Δd_{34} (%)	Δd_{45} (%)	ΔW (eV)	$\Delta\sigma$ (eV \AA^{-2})	$\Delta\sigma_{xx}$ (eV \AA^{-2})	$\Delta\sigma_{yy}$ (eV \AA^{-2})
Experiment	0.0 ^a	−11.4 ^a	−7.7 ^a	11.2 ^a	−5.5 ^a				
LDA	0.6(2)	−7.1(5)	−6.7(5)	6(1)	−3(1)	0.16(3)	0.004(1)	0.00(2)	0.01(2)

For the definition of the symbols see Table 1 and Fig. 3. The workfunction, surface energy and surface tension are given relative to the unreconstructed relaxed surface.

^a From Ref. [2].

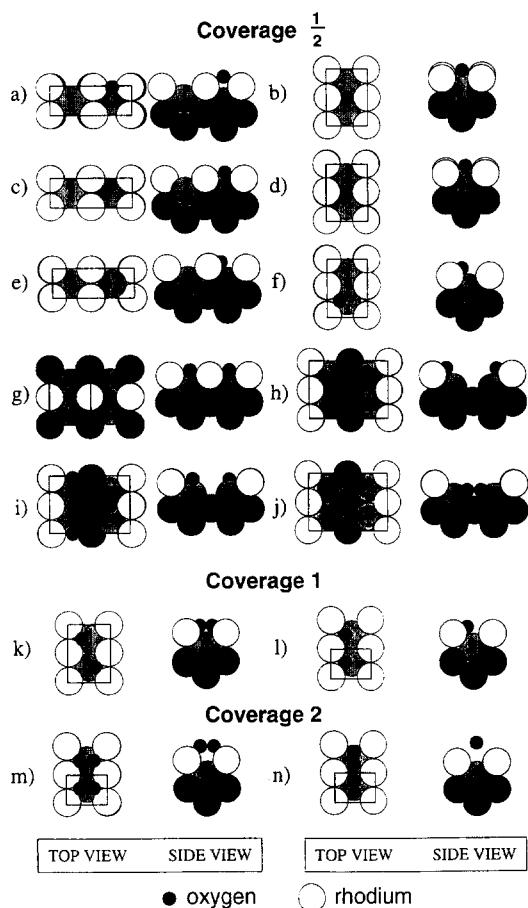


Fig. 4. Relaxed oxygen binding geometries on the Rh(110) surface at coverage 0.5, 1 and 2. The energetically favourable configurations at the three coverages are geometries h, k and m.

surface to the oxygen adsorbate, which for a finite slab affects the Fermi level. However, the finite size effects are much less than those reported for aluminum systems [8], due to the larger number of electrons per atom for the transition metal.

At $\theta=0.5$ we find geometry h to be energetically favoured, while geometry k is favoured for $\theta=1$. The structural data predicted by the present calculations compare well with those determined experimentally [2,3]. The values of the workfunction and the relative chemisorption energy of geometries h and k also compare well with the experimental data. However, the chemisorption energy is overestimated by $\sim 1.2\text{eV}$, which is a typical error of the LDA.

4.1. Coverage 0.5: the unreconstructed surface

We first discuss the stable chemisorption geometries on the unreconstructed rhodium surface at $\theta=0.5$. For the calculations we have used a (2×1) and a (1×2) surface cell and for several different initial positions of the oxygen atom, we have relaxed the structure. We have found six local minima, labeled a, b, c, d, e, and f in Fig. 4. The six oxygen chemisorption sites can be divided into three groups: four-fold coordinated long-bridge sites (geometries a and b), three-fold coordinated quasi-long-bridge sites (geometries c and d), and three-fold coordinated hollow sites (geometries e and f). In the quasi-long-bridge site the oxygen atom has moved away from the long-bridge position towards a second-layer atom in order to obtain three-fold coordination. Note also that the oxygen atom in geometry b sits slightly asymmetric in the long bridge site and must cross a barrier in order to move to geometry d.

The chemisorption energy is highest in the three-fold coordinated hollow site. In these structures most bond lengths between oxygen and rhodium first-layer atoms are nearly 2\AA ; the bonds with second-layer atoms are slightly longer for geometries c, d, e, and f indicating a weaker bond, while there are no bonds with second-layer atoms in geometries a and b. The main difference between the structures is in the bond angle between oxygen and first-layer rhodium atoms, $\theta_{\text{O-1}}$. Inspection of Table 3 shows that the chemisorption energy decreases when the bond angle departs from 90° . In Section 5 we will provide some arguments which indicate why this particular angle corresponds indeed to the strongest oxygen-metal bonds. We also observe that there is almost no inward relaxation of the surface atoms below the oxygen adsorbate.

Based on a HREELS study of the oxygen vibration frequencies for different oxygen coverages of the Rh(110) surface, it was proposed in Ref. [1] that at low coverages oxygen occupies the long-bridge site. This seems to be in disagreement with our calculations, since we find the chemisorption energy in geometry f to be 0.26 eV higher than in geometry a. However, our calculation is for $\theta=$

Table 3

Some key quantities describing the oxygen bonding in the geometries of Fig. 4

Geometry	E_{chem} (eV/O)	$\Delta\sigma/\theta$ (eV/O)	ΔW (eV)	μ (e · Å/O)	$z_{\text{O-1}}$ (Å)	$d_{\text{O-O}}$ (Å)	$d_{\text{O-1}}$ (Å)	$d_{\text{O-2}}$ (Å)	$\theta_{\text{O-1}}$ (°)	$\theta_{\text{O-2}}$ (°)	Δd_{12} (%)
a	1.97(4)	0.23	0.9(1)	0.11(1)	0.94(4)	2.69(1)	1.96(2)	2.77(3)	123(2)	65(2)	–15/10
b	1.86(4)	0.15	0.50(5)	0.056(5)	0.57(3)	3.81(1)	1.99(2)	2.36(3)	147(3)	77(3)	–13/3
c	1.89(4)	0.05	0.51(5)	0.057(5)	0.62(3)	2.69(1)	2.06(2)	2.07(2)	131(2)	80(2)	–14/–2
d	1.94(4)	0.16	0.38(2)	0.044(3)	0.53(1)	3.81(1)	2.03(1)	2.09(1)	140(1)	82(1)	–17/0
e	2.03(3)	0.19	0.40(4)	0.046(4)	0.59(2)	2.69(1)	2.01(1)	2.02(1)	103(2)	87	–11/2
f	2.23(2)	0.11	0.44(5)	0.050(5)	0.71(1)	3.81(1)	2.00(1)	2.05(1)	93(2)	82(1)	–10/–3
g	2.18	1.42	0.50	0.06	0.50	3.81	1.96	2.26	151	79	–1
h	2.75	0.19	0.85	0.10	0.60	3.78	2.00	2.00	85	85	–3
Experiment	1.54 ^a		0.65 ^b	0.074 ^b	0.54 ^c	3.82 ^c	1.98 ^c	1.97 ^c	86 ^c	88 ^c	–1 ^c
Experiment					0.50 ^d	3.89 ^d	2.01 ^d	1.88 ^d	84 ^d	87 ^d	–3 ^d
i	2.26	0.19	0.84	0.10	0.31	4.44	2.02	2.02	(85)	82	–12
j	2.00	0.19	0.14	0.016	–0.61	2.98	(2.02)	(2.06)	(87)	(84)	–6
k	2.23(2)	0.06	0.87(4)	0.049(3)	0.66(1)	2.96(1)	1.99(2)	2.06(2)	85(1)	82(1)	–3
Experiment	1.06 ^a		0.73 ^b	0.041 ^b	0.60 ^c	2.93 ^c	1.98 ^c	2.05 ^c	86 ^c	84 ^c	1 ^c
l	2.06(2)	0.10	0.6(1)	0.034(5)	0.60(2)	2.69(1)	2.00(3)	2.03(3)	85(2)	85(2)	0
m	1.1(1)	0.09	1.4(1)	0.040(4)	1.32(1)	1.32(1)	2.26(1)	2.84(2)	73(1) ^e	64(1) ^e	7
n	–1.1(1)	0.03	–0.65		1.81	1.15	2.74	3.16	88	53	–4

The reported values are: The chemisorption energy E_{chem} , substrate surface energy $\Delta\sigma/\theta$, workfunction (ΔW), oxygen dipole (μ), oxygen–surface distance ($z_{\text{O-1}}$), the shortest bond length with a first layer atom ($d_{\text{O-1}}$), the shortest bond length with a second layer atom ($d_{\text{O-2}}$), the bond angle between bonds with first layer atoms ($\theta_{\text{O-1}}$), the bond angle between bonds with a first layer atom and a second layer atom ($\theta_{\text{O-2}}$), and the first layer relaxation of the rhodium substrate (Δd_{12}) (for the geometries a, b, c, d, e, and f the surface atoms relax differently and we show the value of both the smallest and the largest relaxation). Note that in geometry i the angle $\theta_{\text{O-1}}$ is between the oxygen bonds with second layer atoms, and in geometry j the bond lengths and bond angles are reported for the oxygen bonds with second and third layer atoms. The oxygen dipole-moment was derived from the oxygen-induced workfunction change, and the calculation of the chemisorption energy is described in the Appendix.

^aRef. [41].

^bRef. [4].

^cRef. [3].

^dRef. [2].

0.5, and at this coverage adsorbate–adsorbate repulsions might disfavour certain geometries.

4.2. Coverage 0.5: the reconstructed surface

At $\theta = 0.5$ the annealed surface shows a (2×2) pg LEED pattern [2,3], indicating that the unit cell is (2×2) and must have a glide line in the (110) direction. Furthermore, there is strong experimental evidence that the underlying rhodium substrate forms a (1×2) missing-row structure [2,23]. If we assume that the rhodium atom sits in a three-fold site, there are only three structures consistent with these experimental facts, and these are geometries h, i and j shown in Fig. 4. The same three structures

were considered in the LEED I – V analysis of Ref. [2]. We find geometry h to be energetically favoured, while the oxygen chemisorption energy is 0.5 and 0.8 eV/atom lower in geometry i and j, respectively. Note that the energy ordering of the three structures indicates that oxygen bonds with low coordinated rhodium atoms are energetically favoured. In Table 3 we compare geometry h with two independent LEED I – V structural analyses, and the general agreement is rather good.

Since oxygen induces the (2×1) reconstruction on other transition metal surfaces [24] we have also considered this structure. Initially we placed the oxygen atom in an asymmetrical position above the long-bridge site, but after relaxation oxygen

occupied the symmetrical position 0.4 \AA above the rhodium surface, as shown in geometry g of Fig. 4. We now compare the energetics of this reconstruction with the (1×2) reconstruction. Table 3 shows that while each oxygen atom gains 0.5 eV/atom by forming the (1×2) reconstruction, the (2×1) reconstruction is disfavoured by 0.1 eV/atom . It is interesting to divide this energy into two contributions, the cost of reconstructing the substrate ($\Delta\sigma/\theta$) and the energy gain by bonding oxygen to the reconstructed surface. The formation of the (1×2) reconstruction only costs 0.2 eV/atom (the additional 0.1 eV compared to Table 2 is due to oxygen-induced strain), while the formation of the (2×1) reconstruction costs 1.4 eV/atom . By subtracting the formation energy from the chemisorption energy we see that the oxygen bonding with the (2×1) reconstructed surface is 0.6 eV stronger than the bonding with the (1×2) reconstructed surface. The stronger bonding is due to the lower coordination of the surface atoms, and in Section 5 we will identify the electronic origin of this effect.

Based on the above calculations we now discuss a possible origin of the different reconstructions induced by nitrogen and oxygen on transition metal (110) surfaces. While oxygen induces the (1×2) reconstruction of Rh(110) and the (2×1) reconstruction of Cu(110), Ni(110) and Ag(110) [24], nitrogen has almost the reverse behaviour, i.e. it induces the (2×1) reconstruction of Rh(110) [25] and a (1×3) reconstruction of the Cu(110) and Ni(110) surfaces where every third (110) row is missing [26–28]. To understand this behaviour we have compared the geometry of the theoretical (2×1) reconstruction of O/Rh(110), with the experimentally derived (2×1) structure of N/Rh(110) [25]. The comparison reveals a rather large difference in the adatom–surface distance: while oxygen sits 0.4 \AA above the surface atoms, there is no height difference between nitrogen and the rhodium surface atoms. We propose that an adsorbate positioned exactly in between the surface atom in the (100) row may form the strongest bond, and since nitrogen is a smaller atom than oxygen, it can better fit in between the rhodium surface atoms. This size argument can also explain the preference of oxygen for the (2×1) reconstruc-

tion of silver; since the lattice constant of silver is 4.09 \AA and the O–Ag bond length is 2.05 \AA [29,30], oxygen fits perfectly in between the silver atoms in the (100) row. A similar picture is found for copper, where the lattice constant is 3.61 \AA and the O–Cu bond length 1.81 \AA [24]. The lattice constant of nickel is 3.52 \AA and the O–Ni bond length 1.77 \AA [24], so in this case the oxygen atoms do not fit perfectly in between the nickel atoms, and in Ref. [31] this was identified as a source for lowering the chemisorption energy. Since nitrogen is a smaller molecule than oxygen it forms shorter bonds with the metal atoms, and for copper and nickel the metal–metal separation gets too large for nitrogen to form a strong bond with both metal atoms in the (100) row. However, in the observed (2×3) structure on Cu(110) and Ni(110) it is possible for the surface atoms to relax towards the nitrogen adsorbate, and nitrogen can thereby obtain an optimal bond length with the surface atoms.

4.3. Coverage 1 and 2

For $\theta=1$ we have only studied geometries where the oxygen atom is three-fold coordinated. We find oxygen to have the highest chemisorption energy in geometry k of Fig. 4, in good agreement with experimental findings [3]. The oxygen chemisorption site in geometry k is very similar to that of geometry f, and we also find that the chemisorption energies in the two structures are nearly identical. This suggests that there is little interaction between the oxygen atoms on the Rh(110) surface, which is rather surprising compared to the strong oxygen–oxygen repulsion found on other transition metal surfaces at similar oxygen coverages [32]. In Section 5 we will show that this different behaviour can be explained by a substrate-mediated adsorbate–adsorbate interaction of electronic origin, whose strength is related to the filling of the surface bands.

For $\theta=2$ we have considered two geometries: an oxygen dimer oriented in the (100) direction (geometry m of Fig. 4), and an oxygen dimer oriented in the (110) direction (geometry n). We find geometry m to be energetically favourable, but the chemisorption energy is 1.1 eV lower than

in geometry k. It is therefore questionable whether this structure can be observed experimentally after high oxygen exposure, since the structure will not be energetically favourable compared to geometry k plus molecular oxygen.

Geometrically the main difference between geometry k and geometry m, is the shift of the oxygen bond with a second-layer rhodium atom to an oxygen–oxygen bond. This makes the nature of the oxygen bonding in geometry m somewhat intermediate between those occurring in geometry k and in molecular oxygen. This structure might therefore be an important precursor state for oxygen dissociation.

5. The chemistry of the rhodium–oxygen bond

In this section we will analyse the oxygen chemisorption on rhodium in terms of a simple tight-binding description. A tight-binding model of chemisorption has been put forward by several authors [33–35].

The first step in building a tight-binding description of oxygen chemisorption is to identify the metal and oxygen orbitals which are responsible for the bond formation. For the present problem these consist of all the valence orbitals of rhodium (4d, 5s and 5p) and the O 2p orbitals, while we can disregard the O 2s orbital, since its resonance is ≈ 19 eV below the rhodium Fermi level. As in the model of Refs. [31,36] we describe the interaction between the O 2p orbitals and the metal orbitals in two steps: First the unperturbed orbitals interact with the rhodium Rh 5s and Rh 5p orbitals, and then the resulting renormalized O 2p orbitals interact with Rh 4d orbitals. The different steps are illustrated in Fig. 5. For the unperturbed O 2p state we take the atomic eigenvalue and use the Rh(110) workfunction to position it relative to the rhodium Fermi level ($\epsilon_{2p} - \epsilon_f = -4.1$ eV). We note that the corresponding unperturbed O 2s eigenstate is positioned -18.6 eV relative to the Fermi level, while the fully selfconsistent calculation of geometry f has a O 2s resonance at -18.9 eV. The interaction between oxygen and the broad metal sp bands is similar to the interaction between oxygen and a jellium surface. This interaction is

well described by the weak coupling limit of the Newns–Anderson model, and gives rise to a broadening and a shift of the O 2p level. The interaction between the renormalized O 2p orbitals and the narrow d band is, on the other hand, described by the strong coupling limit of the Newns–Anderson model, and gives rise to a splitting of the levels into bonding–anti-bonding states, similar to the interaction between two atomic orbitals.

By dividing the oxygen–metal interaction into an sp and a d part we obtain a simple picture of the oxygen chemisorption energy on different transition metal surfaces. The interaction with the metal sp bands gives a large contribution to the chemisorption energy, but due to the similarity of the transition metal sp bands, this contribution is more or less constant throughout the transition series. The d band contribution, on the other hand, decreases with the filling of the band, and for the noble metals the O 2p–d anti-bonding level will be filled [36] and in this case there will be a O 2p–d repulsion due to orthogonalization. Fig. 5c schematically shows that the O 2p–Rh 4d anti-bonding level is well above the Fermi level, and the interaction with the rhodium d-band, therefore, gives a large contribution to the chemisorption energy. We note that a substantial part of the O 2p–Rh 4d bond is formed between the O 2p orbitals and localized Rh 4d states with energies close to the Fermi level, i.e. metallic dangling bonds. This is illustrated in Fig. 6 where we show the Rh 4d_{yz} PDOS for both the clean and oxygen covered Rh(110) surface. The figure shows that the 4d_{yz} dangling bond resonance at ϵ_d interacts with the renormalized adsorbate level at ϵ_a and forms a bonding state at $\epsilon_a - \Delta_1$ and an anti-bonding state at $\epsilon_d + \Delta_1$, where $\Delta_1 = \sqrt{\Delta_0^2 + V^2} - \Delta_0$, $\Delta_0 = (\epsilon_d - \epsilon_a)/2$, and V is the O 2p–Rh 4d coupling matrix element.

Since the O 2p level is below the Rh 4d band centre, the bonding state will have mostly O 2p character. There will therefore be a charge transfer from the Rh 4d orbitals into the O 2p orbitals. This charge transfer can be seen in Fig. 7, which shows the charge-density difference between the oxygen+rhodium system and the two separated systems. The plot shows a charge transfer from rhodium orbitals of symmetry $d_{3z^2-r^2}$ (with z along

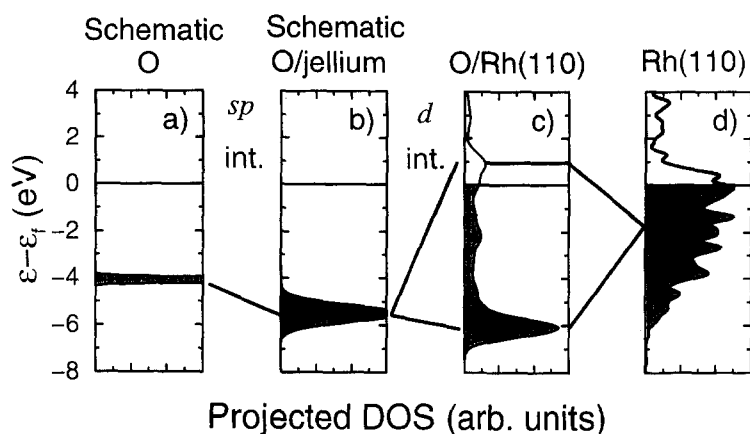


Fig. 5. (a) The atomic O 2p eigenstate. (b) Schematic O 2p PDOS for an oxygen atom coupling to the rhodium 5s and 5p orbitals. (c) The O 2p PDOS of geometry f. (d) The first layer PDOS of the clean Rh(110) surface.

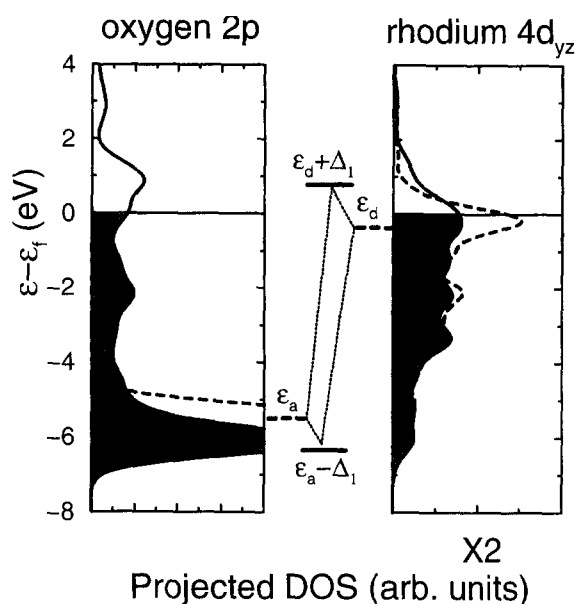


Fig. 6. The DOS of geometry f projected onto the the O 2p orbital and rhodium $4d_{yz}$ orbital. The solid lines show the PDOS of the interacting oxygen–rhodium system, while the dashed lines show the PDOS of isolated oxygen and rhodium systems.

the bond axes) to the O 2p orbitals. We note that the rhodium $d_{3z^2-r^2}$ orbitals have the largest overlap with the the O 2p orbitals, and therefore give rise to the strongest rhodium–oxygen bonds.

In Fig. 8 we show the O 2p PDOS of geometries f and k, and in the spectrum of geometry k we can

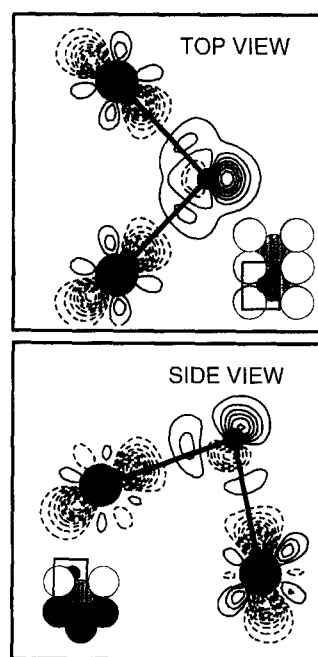


Fig. 7. Contour plot of the oxygen-induced charge-density difference in geometry f. Dashed contour lines indicate charge depletion. The top view shows the charge-density difference in the plane defined by the two first layer rhodium atoms (large grey circles) and the oxygen atom (small solid circle). The side view shows the plane defined by the first and second layer rhodium atoms and the oxygen atom.

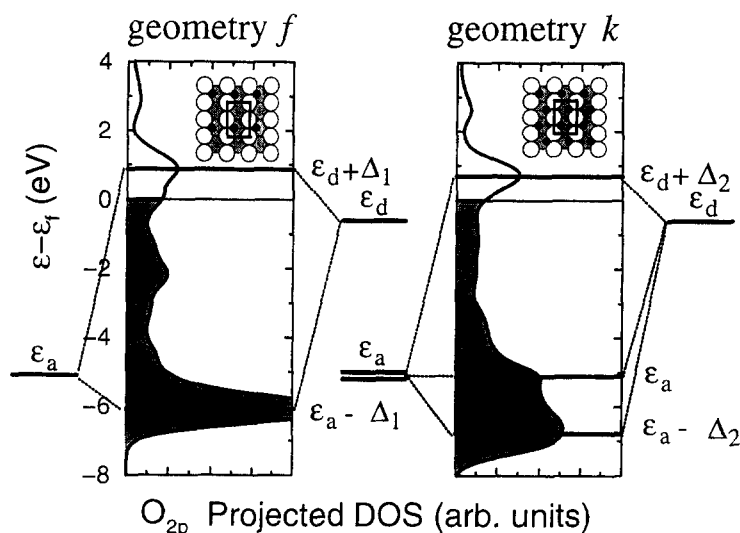


Fig. 8. The O 2p PDOS of geometry f and k. The resonances in geometry f can be described by the bond formation between two levels, ϵ_a and ϵ_d , coupled by V . In geometry k the resonances can be described by the bond formation between three levels, where two levels at ϵ_a are coupled by V to a level at ϵ_d . The level shifts are given by $\Delta_1 = \sqrt{\Delta_0^2 + V^2} - \Delta_0$ and $\Delta_2 = \sqrt{\Delta_0^2 + 2V^2} - \Delta_0$, where $\Delta_0 = (\epsilon_d - \epsilon_a)/2$.

identify 3 resonances. Apparently this is in conflict with the model developed in the previous section which only predicted two resonances, corresponding to the bonding and anti-bonding state of two interacting atomic orbitals. However, in geometry k two O 2p orbitals couple to the same Rh 4d orbital, and the bonding is therefore related to the interaction between three atomic orbitals, which give rise to a bonding resonance at $\epsilon_a - \Delta_2$, an anti-bonding resonance at $\epsilon_d + \Delta_2$, and a non-bonding resonance at ϵ_a , where $\Delta_2 = \sqrt{\Delta_0^2 + 2V^2} - \Delta_0$. From the positions of the three resonances (−6.8 eV, −5.2 eV, and 0.8 eV) we can determine the parameters of the atomic model. We find the renormalized adsorbate level $\epsilon_a = -5.2$ eV, the Rh 4d level $\epsilon_d = -0.8$, and the O 2p–Rh 4d coupling matrix element $V = 2.2$ eV. Compared to the unperturbed adsorbate level ($\epsilon_{2p} - \epsilon_f = -4.1$ eV), the rhodium $4d_{yz}$ resonance of Fig. 6, and the O 2p–Rh 4d coupling matrix element obtained from Harrison's solid-state table [37] $V_{\text{Harr}} = 2.0$ eV, these values seem indeed reasonable. We also note that for two interacting atomic orbitals the parameters predict a bonding resonance at −6.1 eV, in good agreement with the O 2p PDOS of geometry f.

The above chemisorption model gives rise to a strong adsorbate–adsorbate interaction, which can be either attractive or repulsive depending on the position of the metal state ϵ_d relative to the Fermi level. If the metal state is empty ($\epsilon_d > \epsilon_f$) the d-band contribution to the chemisorption energy of non-interacting adsorbates is $E_1 = 2\Delta_1$, while for interacting adsorbates it is $E_2 = \Delta_2$, and since $\Delta_1 > \Delta_2/2$ there is a repulsive adsorbate–adsorbate interaction. However, if $\epsilon_f > \epsilon_d + \Delta_1$ then $E_1 = 0$ and $E_2 = \Delta_2 - \epsilon_f$, and in this case there is an adsorbate–adsorbate attraction. The crossover between repulsive and attractive interaction happens in the range $\epsilon_d < \epsilon_f < \epsilon_d + \Delta_1$, where the difference in the d-band contribution to the chemisorption energy is: $E_2 - E_1 = (\epsilon_d + \Delta_2 - \epsilon_f) - 2(\epsilon_d + \Delta_1 - \epsilon_f)$. From the model parameters we estimate an interaction energy of $E_2 - E_1 = 0.6$ eV, and since two orbitals per oxygen atom contribute to the interaction, the d-band contribution to the chemisorption energy is 1.2 eV larger in geometry k than in geometry f. However, the model also predicts an adsorbate–adsorbate repulsion caused by the O 2p interaction with the almost empty sp band, and since we know from the full self-consistent calculation that the oxygen chemisorption

energy is the same in the two structures, this sp-mediated repulsion must compensate the d-mediated attraction. In geometry 1 of Fig. 4 two neighbouring oxygen atoms can only couple to the same metal s orbital, and there is only an s-mediated repulsion, which gives rise to a 0.2 eV lower chemisorption energy than in geometry 1.

Work is in progress to make the model more quantitative, and preliminary results show that the model can account for the different adsorbate–adsorbate interactions on transition metal and aluminum surfaces [38].

In Section 3 we showed that the bandwidth of the atom PDOS scale is \sqrt{N} , where N is the coordination of the atom, and that there is a corresponding shift of the band centre which conserves the filling of the band. This was illustrated for the Rh(110) surface in Fig. 2, and in the present context we note that the rhodium band centre is shifted upwards. This shift gives rise to a similar shift of the rhodium–oxygen anti-bonding state, and since the bond energy is given by the distance between the anti-bonding state and the rhodium Fermi level the bond is strengthened. The energy gain by the oxygen induced (1×2) reconstruction is therefore due to the oxygen bond with the second-layer rhodium atom, which on the reconstructed surface has coordination 9 and on the unreconstructed surface coordination 11.

6. Conclusions

In this paper we presented detailed first-principles calculations for the clean and half, one and two monolayer oxygen-covered Rh(110) surface. At half monolayer oxygen coverage we find a (1×2) reconstruction of the surface, contrary to the oxygen induced (2×1) reconstruction of Cu(110), Ag(110) and Ni(110), but in good agreement with experimental studies of O/Rh(110). Calculations for the theoretical (2×1) O/Rh(110) structure suggest that this difference in behaviour is related to the scale between the lattice constant and the oxygen–metal bond. Generally the calculations show that the oxygen chemisorption can be rationalized in terms of a tight-binding model which include the O 2p interaction with the rho-

dium valence states. This model give rise to a short-range but strong adsorbate–adsorbate interaction which can be either repulsive or attractive dependent on the filling of the surface bands.

Acknowledgements

We gratefully acknowledge many discussions with K.W. Jacobsen, J.K. Nørskov, R. Rosei and E. Tosatti. Thanks are due to R. Valente for porting our plane-wave ultra-soft pseudopotential program to an IBM-SP2 parallel machine, and to D. Vanderbilt for providing an atomic program for the generation of ultra-soft pseudopotentials. Kurt Stokbro acknowledges financial support from the European Union through HCM contracts ERBCHBGCT 920180 and ERBCHRXCT 930342. This work has been partially supported by the Italian *Consiglio Nazionale delle Ricerche* within the *Supaltemp* project.

Appendix: Calculation of the chemisorption energy

To calculate the oxygen chemisorption energy relative to the O₂ molecule we have used essentially the same procedure as Ref. [8]. With the non-spinpolarized pseudopotential code we have calculated the total energy of the O/Rh(110) system ($E_{O,Rh}$) and the total energy (E_{Rh}) of a relaxed unreconstructed surface using the same super cell, number of atoms and **k**-point sampling. For the chemisorption energy on the reconstructed surface, E_{Rh} is obtained from two slab calculations as in the calculation of the reconstruction energy in Section 3. To find the reference molecular energy we have used an atomic program to calculate the energy E_O^{pol} of a spin-polarized oxygen atom, and from that subtracted the O₂ atomization energy $E_b = 3.74$ eV/atom found by Becke [39]. This value has to be corrected for the use of a finite basis set in the plane-wave calculation, which we estimate to be $E_{pw} = 0.05$ eV/atom. From these energies we calculate the chemisorption energy, E_{chem} , by

$$E_{chem} = E_O^{pol} - E_b + E_{pw} + E_{Rh} - E_{O,Rh}. \quad (A.1)$$

References

- [1] D. Alfe, P. Rudolf, M. Kiskinova and R. Rosei, *Chem. Phys. Lett.* 211 (1993) 220.
- [2] C. Comicioli et al., *Chem. Phys. Lett.* 214 (1993) 438.
- [3] M. Gierer et al., *Surf. Sci.* 297 (1993) L73.
- [4] E. Schwarz, J. Lenz, H. Wohlgemuth and K. Christmann, *Vacuum* 41 (1990) 167.
- [5] P. Hohenberg and W. Kohn, *Phys. Rev.* 136 (1964) B864.
- [6] W. Kohn and L. Sham, *Phys. Rev.* 140 (1965) A1133.
- [7] R. Jones and O. Gunnarsson, *Rev. Mod. Phys.* 61 (1989) 689.
- [8] J. Jacobsen, B. Hammer, K. Jacobsen and J. Nørskov, *Phys. Rev. B* 52 (1995) 14954.
- [9] J.P. Perdew et al., *Phys. Rev. B* 46 (1992) 6671.
- [10] D. Ceperley and B. Alder, *Phys. Rev. Lett.* 45 (1980) 566.
- [11] J. Perdew and A. Zunger, *Phys. Rev. B* 23 (1981) 5048.
- [12] D. Vanderbilt, *Phys. Rev. B* 41 (1990) 7892.
- [13] K. Laasonen et al., *Phys. Rev. B* 47 (1993) 10142.
- [14] K. Stokbro, *Phys. Rev. B* 53 (1996) 6869.
- [15] O.H. Nielsen and R.M. Martin, *Phys. Rev. B* 32 (1985) 3780.
- [16] M. Methfessel and A. Paxton, *Phys. Rev. B* 40 (1989) 3616.
- [17] H.J. Monkhorst and J.D. Pack, *Phys. Rev. B* 13 (1976) 5188.
- [18] WebElements, <http://www.shef.ac.uk/~chem/web-elements/> (University of Sheffield, Sheffield, 1995).
- [19] W.H. Press, S.A. Teukolsky, W.T. Vetterling and B.P. Flannery, *Numerical Recipes in FORTRAN* (Cambridge University Press, Cambridge, 1992).
- [20] W. Nichtl et al., *Surf. Sci.* 188 (1987) L729.
- [21] K.W. Jacobsen, J.K. Nørskov and M.J. Puska, *Phys. Rev. B* 35 (1987) 7423.
- [22] K. Stokbro, N. Chetty, K.W. Jacobsen and J.K. Nørskov, *Phys. Rev. B* 50 (1994) 10727.
- [23] A. Bellman et al., *Surf. Sci.* 298 (1993) 1.
- [24] F. Besenbacher and J.K. Nørskov, *Prog. Surf. Sci.* 44 (1993) 5.
- [25] V.R. Dhanak et al., *Phys. Rev. B* 51 (1995) 1965.
- [26] H. Niehus, R. Spitz, K. Besocke and G. Comsa, *Phys. Rev. B* 43 (1991) 12619.
- [27] F.M. Leibsle, R. Davis and A.V. Robinson, *Phys. Rev. B* 47 (1993) 10052.
- [28] M. Voetz, H. Niehus, J. O'Connor and G. Comsa, *Surf. Sci.* 292 (1993) 211.
- [29] A. Puschmann and J. Haase, *Surf. Sci.* 144 (1984) 559.
- [30] L. Becker et al., *Phys. Rev. B* 44 (1992) 13655.
- [31] K.W. Jacobsen and J.K. Nørskov, *Phys. Rev. Lett.* 65 (1990) 1788.
- [32] D.A. King, in: *Topics in Catalysis*, Vol. 1, Eds. H. Topsøe, M. Boudart and J.K. Nørskov (J. C. Baltzer AG, Basel, 1994) p.315.
- [33] D. Newns, *Phys. Rev.* 178 (1969) 1123.
- [34] R. Hoffmann, *Rev. Mod. Phys.* 60 (1988) 601.
- [35] J.K. Nørskov, in: *Physics and Chemistry of Alkali Adsorption*, Eds. H.P. Bonzel, A.M. Bradshaw and G. Ertl (Elsevier, Amsterdam, 1989).
- [36] B. Hammer and J.K. Nørskov, *Surf. Sci.* 343 (1995) 211.
- [37] W.A. Harrison, *Electronic Structure and the Properties of Solids* (Dover, New York, 1989).
- [38] K. Stokbro, unpublished.
- [39] A.D. Becke, *J. Chem. Phys.* 97 (1992) 9173.
- [40] C. Comicioli, Master Thesis, University of Trieste, Italy, 1991.
- [41] G. Comelli et al., *Surf. Sci.* 260 (1992) 7.